4
Microscale Flow Visualization

Marko Hoffmann, Michael Schlüter, and Norbert Räbiger

4.1
Introduction

Transport phenomena on the microscale have gained particular importance due to an increasing demand for more efficient and sustainable processes. Especially the bridge between nano- and micro technologies requires a deep understanding of multiscale coherences. Advances in microfluidic and nanofluidic technologies have been paralleled by advances in methods for direct optical measurement of transport phenomena on these scales. A variety of methods for microscale flow visualization have appeared and evolved since the late 1990s. These methods and their applications to date are reviewed here in detail, and in the context of the fundamental phenomena that they exploit and the fundamental phenomena that they are applied to measure.

Even if the flow conditions of liquids on the microscale are almost laminar and therefore numerical simulations with high accuracy are applicable, there are several reasons for the basic necessity for experimental flow visualization. In most cases, for instance, the exact data of geometries and wall conditions of microchannels and data on chemical media such as diffusion coefficients and reaction rates are unknown. Furthermore, in cases of chemical reactions, the interaction between mass transport and conversion are not calculable to date, especially if simultaneous catalytic processes take place. Therefore, the visualization of microscale flow is a helpful tool for understanding and optimizing microchannels.

Driven by increasing computer power and basic research in microbiology, rapid development in spatial and temporal high-resolution measuring techniques occurred during the last decade. Particle image velocimetry (PIV) and confocal laser scanning microscopy (CLSM) have become common tools for studying phenomena on the microscale. This chapter gives an introduction to common visualization techniques for microscale flow and provides some information on their applicability and limits.

Micro Process Engineering, Vol.1: Fundamentals, Operations and Catalysts
Edited by V. Hessel, A. Renken, J.C. Schouten, and J.-I. Yoshida

ISBN: 978-3-527-31550-5

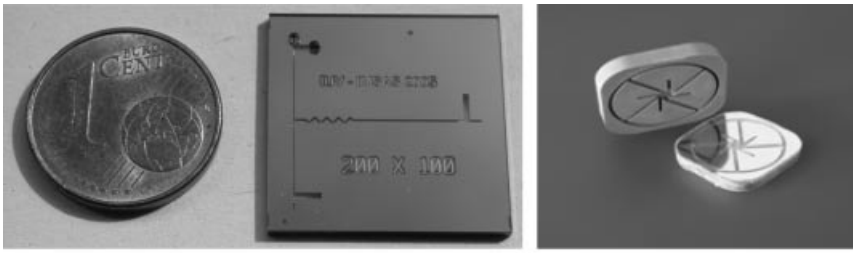

Figure 4.1 Microchannel fabricated in silicon with a bonded glass lid (a) and micromixer fabricated in micro metal injection molding with glued glass lid (b).

4.2 Fundamentals

Most measurement techniques for microscale flow visualization make use of a microscope to obtain appropriate spatial resolution. Therefore, optical access is necessary in order to allow a view into the channel without influencing the flow conditions. In most cases, microchannels can be covered by a glass lid, whereas more complex geometries require special solutions. Depending on the material and geometry of the channel, the glass lid can be bonded, glued or sealed with a gasket (Figure 4.1).

For the illumination of the flow, a laser beam is introduced into the microchannel which passes the lenses of the microscope displaced from the optical axis. Special attention should be paid to the working distance between the glass lid and objective, which depends on the numerical aperture (*NA*) of the objective, defined as

$$NA = n \sin \alpha \tag{4.1}$$

where n is the refractive index of the immersion medium used between the objective and the object ($n = 1$ for air; $n = 1.51$ for oil or glass) and α is half of the opening angle of the objective (Figure 4.2).

Therefore, the objective needs to be positioned within a distance of a couple of millimeters from the glass lid. Furthermore, the glass lid has to be light-transmissive

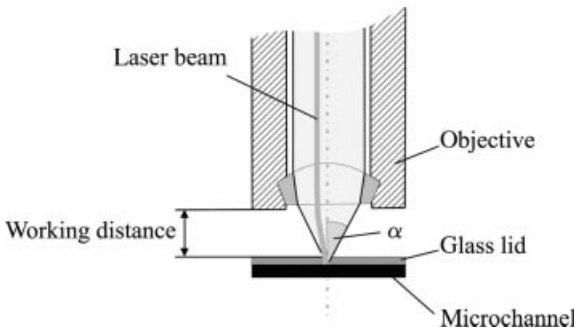

Figure 4.2 Setup for microscale flow visulization.

for the excitation and emission wavelengths. For objectives of high aperture used without immersion oil, the glass lids should have the standard thickness of 0.17 mm, since here the cover glasses are already taken into account in the complicated computation of objectives. Therefore, if a different thickness than the standard one is used, the quality of the optical image suffers visibly in the case of high apertures. If available, an objective with a correction collar should be used. These objectives can be adapted seamlessly to various optical conditions, e.g. a cover glass thickness up to 1.5 mm. More details on modern microscopy can be found in [1].

For the measurement of velocity fields, tracer particles are added to the flow. These are usually labeled with a fluorescent dye for a more intensive illumination in laser light (PIV). For the measurement of concentration fields, a fluorescent dye is dissolved in the liquid whereas the concentration of dye corresponds to its fluorescence intensity.

4.3 Visualization of Flow Fields in Micro- and Minichannels

In order to visualize the velocity field, microparticle image velocimetry (μ-PIV) and microparticle tracking velocimetry systems have been well applied in the last 10 years. If a microscale fluid flow has a 3D characteristic, e.g. in a T-shaped micromixer at higher *Re* (Reynolds number), the two-dimensional and two components (2D + 2C) μ-PIV is limited. Derived from macroscale flow mapping methods, several measurement techniques have been further developed to capture the 3D flow features in microscale fluid flows. These measurement techniques are holographic PIV, defocusing digital PIV and stereoscopic PIV.

4.3.1 Microparticle Image Velocimetry (μ-PIV)

During the last decade, remarkable progress has been made in the development and application of micron-resolution particle image velocimetry (μ-PIV). While typical spatial resolutions for macroscale PIV are 1 mm, the spatial resolution for μ-PIV could be reduced to the order of 1 μm. These advances have been obtained as a result of remarkable improvements in instrument hardware and post-processing software. The utility includes the application to flows in micro- and minichannels, micronozzles, BioMEMS and flows around cells. While this technique was initially developed for microscale velocity measurements, it has been extended to measure wall positions with a tens of nanometers resolution, the deformation of hydrogels, microparticle thermometry and infrared PIV. Whereas most conventional PIV investigations make use of light sheet illumination, they are not a practical source of illumination for microfluidic flows, due to a lack of optical access along with significant diffraction in light sheet forming optics [2]. As a consequence, the flow must be volume illuminated. The visualization of the seed particles is carried out with an optical system whose depth of field exceeds the depth of the flow being measured

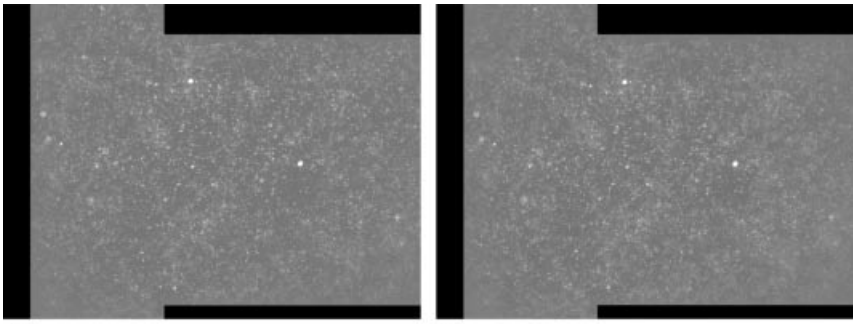

Figure 4.3 μ-PIV raw image: T-shaped micromixer; mixing channel width = 400 μm, inlet channel width = 200 μm; image 1: t_1 (a); image 2: $t_2 = t_1 + \Delta t$ with $\Delta t = 2\,\mu s$ (b).

or, most commonly used, with an optical system whose depth of field is small compared to that of the flow.

The most common mode of PIV is to record two successive images of flow tracing particles that are introduced into the working fluid and accurately follow the local motion of the fluid. Therefore, the particles should have nearly the same density as the working fluid and a sufficiently small particle diameter d_p to ensure a high spatial resolution and trajectories that faithfully follow the flow in microfluidic devices, which often exhibit high velocity gradients near flow boundaries. The two particle images are separated by a known time delay Δt, mostly in the range of microseconds. The local velocity of the fluid u is given by

$$u = \frac{\Delta x}{\Delta t} \tag{4.2}$$

with the measured displacement Δx of the particles between both images.

Figure 4.3 shows a typical raw image pair for a flow with Reynolds number $Re = 186$ within the entrance region of a T-shaped micromixer with $400 \times 200\,\mu m^2$ cross-section of the mixing channel. In this case polystyrene particles with a diameter $d_p = 500$ nm coated with Rhodamine B are illuminated with a double-pulsed Nd:YAG laser, pulse width 5 ns. The time interval between both frames is 2 μs. To evaluate the most probable local displacement Δx for a ensemble of particles, the two particle image fields are divided into uniformly spaced interrogation regions with a common size of 16×16, 32×32 or 64×64 pixels and cross-correlated with the following methods.

4.3.1.1 Correlation Averaging Method

For correlation-based PIV evaluation algorithms, the correlation function at a certain interrogation spot is calculated according to

$$\Phi_k(m,n) = \sum_{j=1}^{q} \sum_{i=1}^{p} f_k(i,j) \cdot g_k(i+m, j+n) \tag{4.3}$$

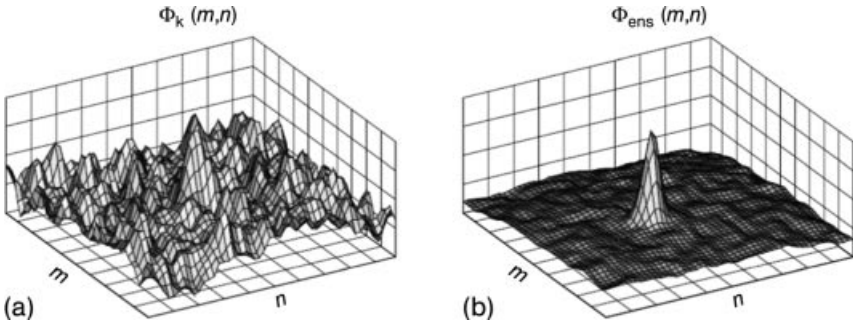

Figure 4.4 Effect of ensemble correlation: (a) conventional cross-correlation for one of the PIV recording pairs; (b) results with ensemble correlation for 101 PIV recording pairs [3] (by courtesy of Springer-Verlag).

where $f_k(i, j)$ and $g_k(i, j)$ are the gray value distributions of the first and second exposure, respectively, in the kth PIV recording pair at a certain interrogation spot of size $p \times q$ pixels.

The correlation function for a singly-exposed PIV image pair shows a peak at the position of the particle image displacement in the interrogation spot (or window), which should be the highest among all the peaks of Φ_k (see Figure 4.4b). If there is, for instance, too much noise or mismatch of particle images, the main peak will become weak and may be lower than some of the "sub"-peaks, and as such, an erroneous velocity vector is generated. For common laminar and stationary flow conditions in microfluidic liquid flow, the velocity field is independent of measurement time. Hence the main peak Φ_k (m, n) is always at the same position for PIV recording pairs taken at different times while the sub-peaks appear with random intensities and positions in different recording pairs.

Therefore, when averaging Φ_k over a large number of PIV recording pairs (N), the main peak will remain at the same position in each correlation function but the noise peaks, which occur randomly, will average to zero (Figure 4.4).

The averaged (or ensemble) correlation function, as implemented in many PIV software tools, is given as

$$\Phi_{\text{ens}}(m, n) = \frac{1}{N}\sum_{k=1}^{N} \Phi_k(m, n). \tag{4.4}$$

The result of the cross-correlation for the above given raw images (Figure 4.3) is given in Figure 4.5 that shows the typical 2D + 2C velocity field inside the entrance region of a T-shaped micromixer as a horizontal slice in the middle of the channel, i.e. at half the channel depth. Due to sufficient particle seeding and high signal-to-noise ratio, the "normal" cross-correlation was used with a interrogation size of 32×32 pixels and half-overlapping.

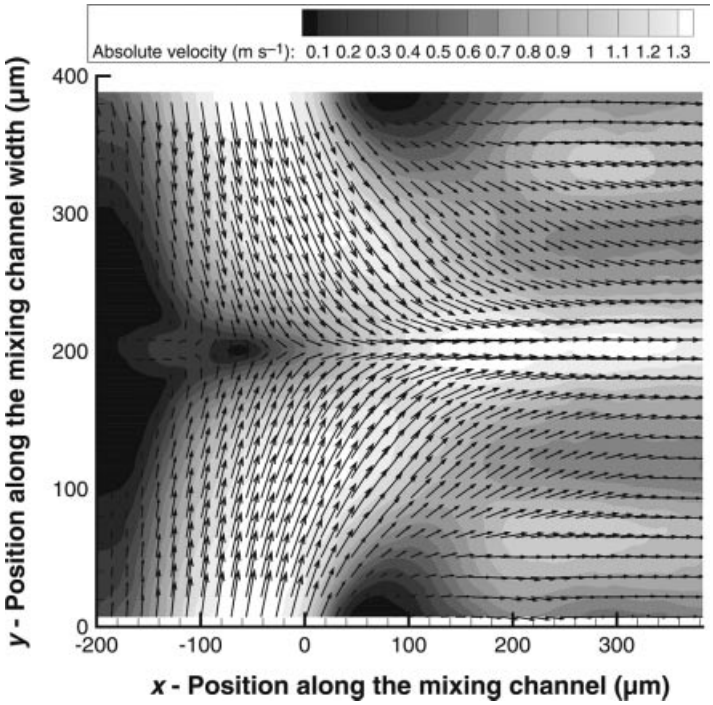

Figure 4.5 Velocity field–entrance region of a T-shaped micromixer [4].

4.3.1.2 3D Reconstruction

It is also possible to calculate the out-of-plane velocity component w from the two in-plane components u and v by using the continuity equation, Equation (4.5), for incompressible flow, as shown in [5] for a turbulent flow around a surface-mounted obstacle.

$$\frac{\partial u_i}{\partial x_i} = 0 \quad \text{with} \quad x_i = (x, y, z); \quad u_i = (u, v, w) \tag{4.5}$$

Integration of Equation (4.5) in the z-direction (out-of-plane) yields the expression to gain the w component:

$$w(x_i, y_j, z_k) = w(x_i, y_j, z_{k-1}) - \int_{z_{k-1}}^{z_k} \left[\frac{\partial u}{\partial x}(x_i, y_j, z) + \frac{\partial v}{\partial y}(x_i, y_j, z) \right] \mathrm{d}z \tag{4.6}$$

discretized in the nodes i, j, k, of a three-dimensional (measurement) grid. The derivatives in the integral of Equation (4.6) were computed in the x,y,-plane, employing (second-order) central differences.

This technique for calculating the out-of-plane component was recently applied to microfluidic flows [4, 6]. With the knowledge of the third velocity component w it is possible to visualize the 3D structure in the entrance region of a T-shaped micromixer, as shown in Figure 4.6. The out-of-plane component w is unequal to zero,

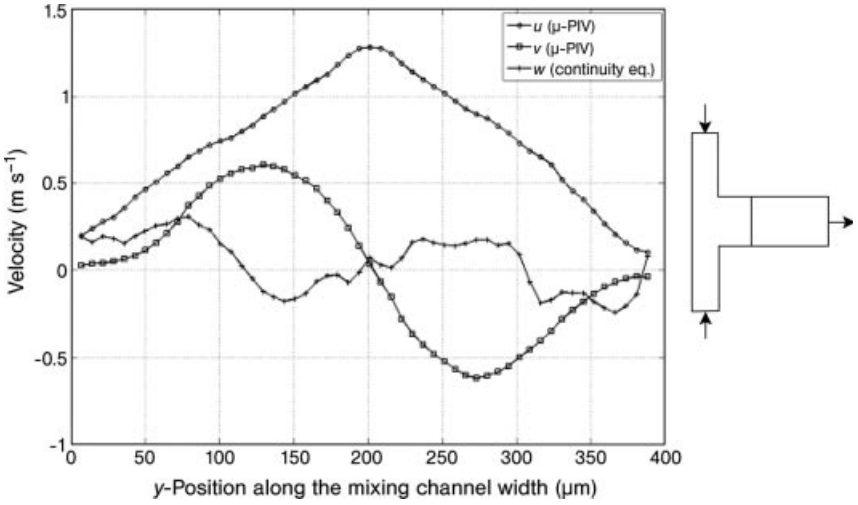

Figure 4.6 Velocity components *u*, *v*, *w*, entrance region of a T-shaped micromixer; out-of-plane component *w* is calculated by means of the continuity equation [4].

indicating that the flow structure is three-dimensional in the entrance region of this type of mixer [4].

4.3.1.3 Accuracy of μ-PIV Measurements

The measurement error of μ-PIV measurements due to detectability ε_d is given by the ratio of the uncertainty of the correlation peak location δ_x to the particle displacement Δx

$$\varepsilon_d = \frac{\delta x}{\Delta x} \tag{4.7}$$

For a commonly used objective lens 20×/0.5 and a particle diameter $d_p = 0.5\,\mu m$, the uncertainty of the correlation peak location δx is given by $\delta_x = d_e/10\,M = 134\,nm$.

If the particle image resolution obtained by the CCD array of the camera is sufficient (3–4 pixels), the location of the correlation peak (Figure 4.4) can be resolved to within one-tenth of the particle image diameter d_e [7]. This makes it clear that the effective particle image diameter d_e determines the lower limit concerning the spatial resolution that can be achieved. The effective particle image diameter d_e can be calculated according to Adrian and Yao [8] by the equation

$$d_e = [{d_s}^2 + M^2 {d_p}^2]^{\frac{1}{2}} \tag{4.8}$$

with magnification M and particle diameter d_p. The diffraction-limited spot size d_s can be calculated according to Adrian [9] by

$$d_S = 2.44(M+1)f^{\#}\lambda \tag{4.9}$$

with the *f*-number of the lens $f^{\#}$ and the wavelength of light λ.

The *f*-number for the most common infinity-corrected microscope objective lens is given by

$$f_{\infty}^{\#} = \frac{1}{2}[(n/NA)^2 - 1]^{\frac{1}{2}} \tag{4.10}$$

with the refractive index n of the immersion medium between objective lens and object. These infinity-corrected optical systems are often used in μ-PIV to record submicron particles with a relatively high magnification because they allow an adjustable distance between objective lens and relay lens without affecting the magnification. In addition, optical filters and mirrors can be inserted between the lenses without distorting the image [10].

The most common microscope objectives range from diffraction-limited oil-immersion objectives ($M = 60$; $NA = 1.4$) to air lenses ($M = 10$; $NA = 0.1$). An overview of the effective particle image diameter d_e for different magnifications and numeric apertures is given in [3].

For the stated objective $20\times/0.5$ and an error $\varepsilon_d = 2\%$, the required particle displacement is 6.7 μm. It is obvious from Equation (4.7) that a compromise must be found between the spatial resolution and the accuracy of the velocity measurements. To obtain a small effective particle image diameter d_e, high numerical aperture diffraction-limited optics and a sufficiently high magnification should be used [3].

4.3.1.4 Depth of Correlation

The depth of the field for a volume-illuminated μ-PIV setup does not define precisely the thickness of the measurement plane because only the sharply focused particles contribute to the correlation function. The depth of the field is defined as twice the distance from the object plane to the plane in which the object is regarded as unfocused. The depth of correlation depends on the axial distance Z_{corr} from the object plane in which a particle becomes sufficiently out of focus so that it no longer contributes significantly to the peak in the particle-image correlation function and can be calculated according to

$$z_{corr} = \left(\left(\frac{1-\sqrt{\epsilon}}{\sqrt{\epsilon}} \right) \left\{ \frac{{d_p}^2[(n/NA)^2 - 1]}{4} + \frac{1.49(M+1)^2\lambda^2[(n/NA) - 1]^2}{4M^2} \right\} \right)^{\frac{1}{2}} \tag{4.11}$$

The relative contribution ϵ of a particle displaced the distance $z = z_{corr}$ from the object plane compared with a similar particle located within the object plane $z = 0$ can be calculated according to Wereley and Meinhart [3] with the effective particle image diameters $d_{e\,(z=0)}$ and $d_{e(z=z_{corr})}$ of the particles according to

$$\varepsilon = \frac{{d_{e(z=0)}}^4}{{d_{e(z)}}^4} \tag{4.12}$$

Following the analysis of Olsen and Adrian [11], the effective image diameter of a particle d_e displaced a distance z from the objective plane can be approximated by

combining Equations (4.9) and (4.8) and including a third term to account for the geometric spreading of a slightly out of focus particle. The effective diameter changes according to

$$d_e = \left\{ M^2 {d_p}^2 + 1.49(M+1)^2 \lambda^2 [(n/NA)]^2 - 1 + \frac{M^2 D_a^2 z^2}{(s_0 + z)^2} \right\}^{\frac{1}{2}} \tag{4.13}$$

with the distance s_0 and the diameter D_a of the recording lens aperture. In most publications the relative contribution is assumed between $\epsilon = 0.01$ and 0.1 (e.g. [3, 11, 12]).

It thus becomes clear that the depth of correlation is strongly dependent on the numerical aperture *NA*, the particle diameter d_p and to a lesser extent the magnification *M*. As an example for a $20\times/0.5$ objective and a particle size $d_p = 0.50\,\mu m$, the depth of correlation is $2\,z_{corr} = 7\,\mu m$. An overview of the thickness of the measurement planes for commonly used objectives is presented in [3].

4.3.1.5 Brownian Motion

Brownian motion is the random thermal motion of a particle suspended in a fluid. This motion results from collisions between fluid molecules and suspended particles. For time intervals Δt much larger than the particle inertial response time, the dynamics of Brownian motion are independent of inertial parameters such as particle and fluid density. The Brownian diffusion coefficient *D* is given by the Stokes–Einstein equation as

$$D = \frac{\kappa T}{3\pi\eta d_P} \tag{4.14}$$

where d_p denotes the particle diameter, η the dynamic viscosity, κ the Boltzmann constant ($1.38 \times 10^{-23} J\ K^{-1}$) and *T* the absolute temperature.

The relative errors ϵ_x and ϵ_y as a result of visualizing the Brownian particle displacement in two dimensions are given by

$$\epsilon_x = \frac{\sigma_x}{\Delta x} = \frac{1}{u}\sqrt{\frac{2D}{\Delta t}} \quad \text{and} \quad \epsilon_y = \frac{\sigma_y}{\Delta_y} = \frac{1}{v}\sqrt{\frac{2D}{\Delta t}} \tag{4.15}$$

It is obvious that this Brownian error establishes a lower limit concerning the measurement time interval Δt. For shorter times, the measurements are dominated by uncorrelated Brownian motion. Brownian motion becomes an important factor when tracing 50–500 nm particles in flow field experiments with flow velocities of less than about $1\,mm\,s^{-1}$. For a velocity of $0.5\,mm\,s^{-1}$ and a seed particle diameter $d_p = 500\,nm$, the lower limit is $\Delta t \approx 100\,\mu s$ for an error of 20% due to Brownian motion. It is possible to reduce this error by averaging over several particles in a single interrogation spot and by ensemble averaging over several realizations [3]. On the other hand, Equation (4.15) shows that the effect of Brownian motion is relatively less important for faster flows.

4.3.2 Extension of Common μ-PIV for Enhancement of Spatial and Temporal Resolution

One of the most important challenges in μ-PIV in recent years concerns the enhancement of spatial resolution in axial direction by reducing the measurement depth.

One method to reduce the measurement depth was applied by Mielnik and Saetran by using a selective seeding of a thin fluid layer within an otherwise particle-free flow [13]. In analogy with the laser sheet in macroscale PIV, the generated particle sheet defines both the depth and the position of the measurement plane, independent of the details of the optical setup. Mielnik and Saetran used selectively seeded μPIV to measure the instantaneous velocity field in a microchannel with a depth-wise resolution of 20% below the estimated optical measurement depth of the μ-PIV system. Mielnik and Saetron supposed that a measurement depth corresponding to the diameter of the tracer particles can be achieved [13].

Another possibility for specifying the measuring depth more precisely is to utilize the defocusing effect of fluorescent particles. Luo *et al.* achieved a distinct defocusing of fluorescent particles by using an air immersion objective ($M = 40$, $NA = 0.6$) and a thick glass cover with a mismatched refractive index [14]. These non-design optical conditions cause diffraction patterns of the sub micron fluorescent particles changing with the defocus distance out of the front focal plane in the optical axis direction. The diffraction patterns can be applied for various optical conditions with a scalar diffraction model to analyze and determine the defocus distance of the particle. According to Luo *et al.*, a submicron accuracy is reachable with this technique [14].

For higher temporal resolution of microscale flow visualization, high-speed CCD cameras and lasers with high pulse repetition frequencies or powerful continuous wave lasers are gaining increasing interest. These high-speed μ-PIV techniques have become more and more applicable to the investigation of transient phenomena in microfluidic devices. Shinohara *et al.* combined a high-speed camera and a continuous wave laser to measure a micro-countercurrent flow of water and butyl acetate in a microchannel. The velocity fields of water in the microcounter current flow were visualized with a temporal resolution of 500 μs and a spatial resolution of $2.2 \times 2.2\,\mu m^2$. According to Shinohara *et al.*, vortex-like motions of fluorescent particles become visible along the water–butyl acetate interface with this technique [15].

4.3.2.1 Multiphase Flow

For many chemical and biochemical applications, e.g. homogeneous catalysis, hydrogenation, oxidation, fermentation or biomedical analysis of an additional liquid, a solid or gaseous phase is necessary within the microchannel. Even though the dominant surface effects of dispersed phases may cause problems with plugging in microchannels, the advantage of mixing enhancement within single slugs is initiating a speedy development of multiphase applications for microchannels [16–21].

Several groups have visualized the flow field within a multiphase flow in microchannels using μ-PIV [22]. The experimental setup is similar to that described in

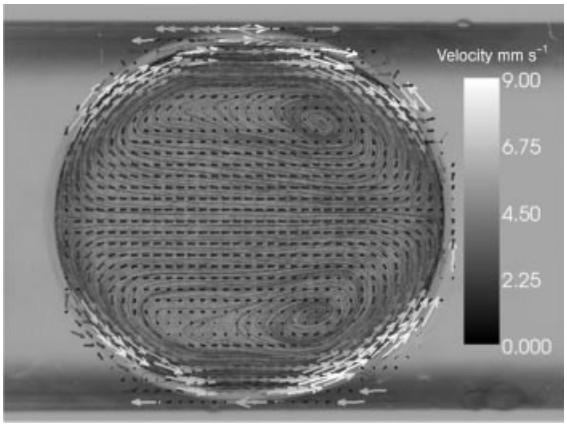

Figure 4.7 Reversed symmetrical flow fields are induced by the translation of microdroplets through linear microchannels (transport velocity: 7.6 mm s^{-1}). Due to symmetry, mass transfer between the lower and upper half of the segment is repressed and thus mixing has declined considerably. The measured internal flow inside a microdroplet is displayed for a microchannel with dimensions of 780 × 260 μm^2. Internal flow is induced at the liquid/liquid interface with four regions of maximum flow. Adapted from [22] (by courtesy of Elsevier).

Section 4.3.1. The main difference is the moving target within the channel. To achieve a more dynamic range of detectable velocities it might by useful to apply a Reynolds decomposition by subtracting the mean velocity of the slugs from the measured velocities within the moving particles as given by Adrian *et al.* for turbulent flows [23].

A recent study by Malsch *et al.* [22] involved μ-PIV to characterize two-phase flows in microchannels. This method has been developed and introduced to measure internal flows in large segments and also in small segments to investigate the contribution of interface friction to the formation of the internal flow field. To distinguish between the phase internal flow and the global flow field of the segment translating through the microchannel, segments from both frames have to be transformed into the same coordinate system with a segment matching algorithm before PIV analysis. The result of this method is the phase internal flow field.

The results obtained from μPIV analysis are presented in Figure 4.7, in this case the translation of microdroplets through linear microchannels (transport velocity 7.6 mm s^{-1}). For small segments, the contribution of the liquid/liquid friction to the phase internal flow is determinant and liquid/wall friction is minimal due to its low interface area. As Figure 4.7, shows, the flow field is symmetrical with respect to the channel direction. Impulse transfer occurs at the four regions with maximum flow at the interface [22].

4.3.3
Confocal Microparticle Image Velocimetry

For more sophisticated applications of μ-PIV, the enhancement of spatial resolution is only achievable with a confocal microscope. Most confocal microscopes, however,

use scanning laser technology for image acquisition. This scanning laser severely lacks the temporal resolution required to monitor dynamic microscale flows. A possibility for avoiding this disadvantage is to use a spinning disc confocal microscope. The spinning disc (Nipkow disc) consists of a thin wafer with hundreds of pinholes that are arranged in a spiral pattern. When a portion of the disc is placed in the internal light path of the confocal microscope, the spinning disc produces a scanning pattern of the subject. As the subject is inspected, light is reflected back through the microscope objective. The pinholes of the disc permit only perpendicularly oriented rays of light to penetrate. This enables the microscope to view a very thin optical section of the target at extremely high speeds because it is not limited by the speed of the scanning laser.

For example, Lima *et al.* combined a conventional PIV system with a spinning disc confocal microscope to obtain high-resolution images and 3D optical section velocity measurements in order to determine the influence of suspended blood cells on the flow behaviour. Lima *et al.* suggested, based on the good agreement between the measured and estimated results, that macroscale flow theory can be used to predict the flow behavior of a homogeneous fluid within a $100\,\mu m^2$ square microchannel. These results also demonstrate the potential of the confocal system for generating 3D profiles and consequently obtaining detailed information on microscale effects in microchannels using both homogeneous and non-homogeneous fluids, such as a suspension of blood cells [24].

Another application for high-speed confocal μ-PIV was given by Kinoshita *et al.*, who presented a microflow diagnostic technique for the internal flow of a droplet passing through a microchannel. The confocal μ-PIV system allows a temporal resolution of 2000 frames s^{-1} in a $228 \times 171\,\mu m^2$ region with a confocal depth of 1.88 μm. Kinoshita *et al.* proposed a three-dimensional velocity measurement method based on confocal μ-PIV and the continuity equation [25].

4.3.4
Stereoscopic Microparticle Image Velocimetry

Closely following the experimental setup used for macroscale stereoscopic PIV, Bown *et al.* developed a stereoscopic μ-PIV system based on stereomicroscopy with a stereomicroscope. Two cameras captured particle images from two different angles simultaneously. Vector fields of images from each angle were then obtained by the 2D PIV method and three-dimensional velocity vectors were calculated by recombining the two vector fields from different angles [26]. One of the challenges in stereoscopic μ-PIV is the calibration. Bown *et al.* used a simple optical model of the stereomicroscope for the calibration in their first measurement. The second measurement was calibrated using an image of a calibration target outside the microchannel and a parameter fit with a direct linear transformation (DLT). The authors emphasized that a calibration outside the microchannel is erroneous. The depth of correlation in their measurements was 56 μm. On the other hand, Lindken *et al.*, who firstly introduced the stereoscopic μ-PIV system, described the development of a stereoscopic μ-PIV system with a calibration of the two image planes in a closed microchannel by means

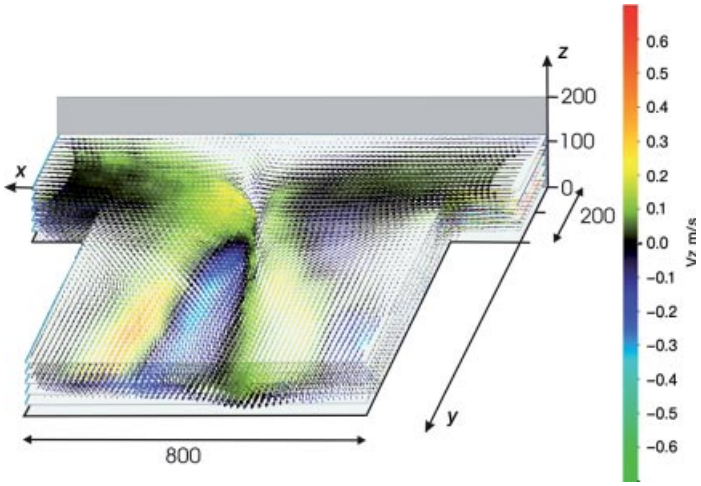

Figure 4.8 Three-dimensional velocity field of stereo-μ-PIV measurements in the mixing zone of a T-shaped micromixer at $Re = 120$. The flow is laminar and stationary. The in-plane velocity distribution is presented as vectors and the out-of-plane component of the velocity, z-component is displayed colour coded. Only the lower half of the 3D scan from $z = 22$ to 100 μm in the center of the channel of the $800 \times 200\,\mu m^2$ cross-section is shown [12] (by courtesy of Springer-Verlag).

of a so-called self-calibration using the particle images [12]. They presented test measurements for determining the accuracy of the method and first measurements of the laminar, 3D flow in a T-shaped micromixer, (Figure 4.8).

4.3.5
3D Particle Tracking Velocimetry

Recently, Kim and Lee developed a microdigital holographic particle tracking velocimetry (HPTV) system with a high-speed digital camera for measuring the temporal evolution of 3D velocity fields of micro/bio fluid flows. They applied this microdigital HPTV to measure instantaneous 3D velocity vectors of flow in a microtube with differing particle number densities and flow rates [27]. Yang and Chuang advanced a hybrid multiplexing holographic velocimetry system for characterizing 3D and three-component (3D + 3C) flow behaviors in microscale devices. In this case, 3D + 3C velocity data for the flow behind a backward-facing step [28] are obtained.

Further publications have presented microscopic methods for the 3D determination of the velocity distribution in microchannels by means of the 3D point spread function (PSF). With defocus, the spot diameter of a nanoparticle first increases, and then for larger displacements from the focus complex ring intensity patterns are developed. The full 3D pattern represents the PSF of the optical system and is determined mainly by the objective lens of the microscope system. The intensity pattern, i.e. the number and diameter of rings and the relative intensity of rings, gives information about the distance of the object from the imaging focal plane. Speidel

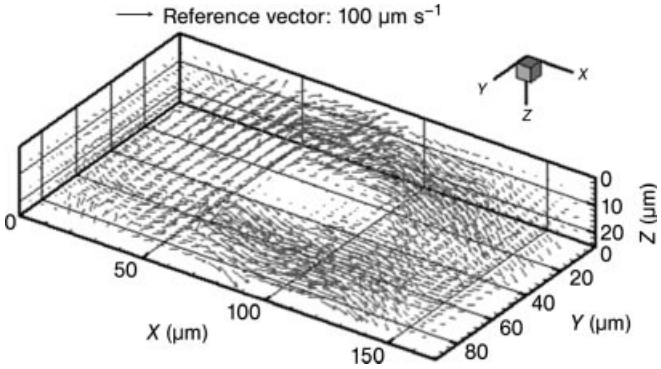

Figure 4.9 Measured 3D vector fields [31] (by courtesy of Springer-Verlag).

et al. tracked 216 nm latex particles in three dimensions based on the size and shape of the circular diffraction rings of defocused image particles. Because a calculated PSF is not accurate enough, they determined the 3D PSF experimentally [29]. By using a computed PSF, Wu *et al.* tracked bacteria in water with the same procedure [30].

With an epi-fluorescent microscope, a dry objective lens (40×, $NA = 0.75$) and fluorescent particles with a diameter $d_p = 500\,\text{nm}$, a single-camera μ-PTV technique using the described deconvolution microscopy has been developed by Park and Kihm [31]. In this case, only the outermost diffraction pattern ring size variations of defocused particle images are compared with a computed PSF. With this technique, it is possible to map simultaneously the three-component velocity vectors for 3D microscale flow fields. The measured 3D vector fields for the creeping flow over a 95 μm diameter sphere inside a nominal $100\,\mu\text{m}^2$ square channel is shown in Figure 4.9.

4.4 Visualization of Concentration and Temperature Fields in Micro- and Minichannels

Scalar-based flow velocimetry, where the motion of the bulk fluid is inferred from the observed velocity of a conserved scalar, has been widely applied in fluid mechanics from the work of Reynolds (1883) to the present for macro- and microscale applications [32]. The basis is the use of light emitting molecules (fluorescent or phosphorescent). In this section the laser-induced fluorescence (LIF) measurement technique will be discussed in detail. This technique tags one of the liquids by a fluorescent dye and records the fluorescence intensity originating from that dye, which is linked to the concentration of the respective liquid. In contrast to the application of fluorescence intensity techniques to macroscopic flows (LIF), the present application to microflows does not allow one to span up a light sheet and instead illuminates the complete microchannel volume.

In order to measure the concentration field, the inlet stream contains the fluorescent dye Rhodamine B (dissolved in a pH 8.2 buffer solution). The fluores-

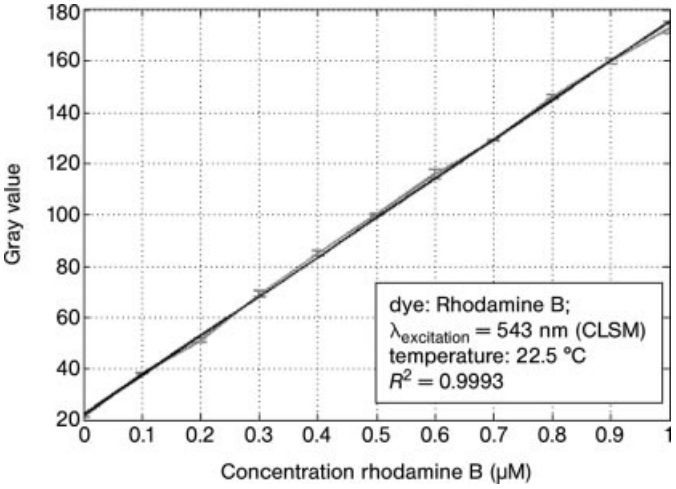

Figure 4.10 Calibration gray value vs fluorescence dye concentration (Rhodamine B); each measuring point: mean gray value and standard deviation for 50 vertical slices [4].

cence intensity of the fluorochrome I_f is proportional to the intensity of the light absorbed by the dye I. This intensity I is calculated by the Lambert–Beer law.

$$I_f = \phi I = \phi I_0 e^{-\epsilon bc} \tag{4.16}$$

where the intensity of the exciting light is I_0, ϵ is the molar extinction coefficient (e.g. for Rhodamine B 108 000 $cm^{-1} mol^{-1}$), ϕ is the quantum yield and describes the effectiveness of the fluorescent emission (e.g. for Rhodamine B $\phi = 0.97$) and b is the length of the measurement volume.

For low concentrations, e.g. 1μ mol^{-1}, the intensity of the light emitted by the fluorescent dye Rhodamine B is linearly dependent on the concentration of the dye [Equation (4.16) can be simplified by a series expansion so that I_f is proportional to the concentration c of the dye, Figure 4.10] [33].

4.4.1 Analysis of Concentration Fields

In addition to the determination of the fluid velocity in microchannels, there have been recent developments in scalar-based visualization methods for micromixers. The use of regular fluorophores such as fluorescein or Rhodamine B is very common in direct visualization of mixing in microfluidic devices.

Ito and Komori used a vibration technique for promoting fluid mixing and a chemical reaction in a microchannel [34]. Instantaneous velocity and concentration fields are measured using μ-PIV and μ-LIF techniques, respectively, whereas the concentration measurement takes place in a non-reacting flow with the dye Rhodamine B. The effects of mechanical vibration on mixing and reaction were experimentally examined. The fluids were oscillated by a small vibrating motor through two

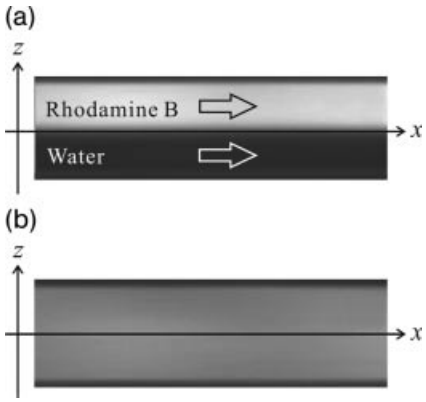

Figure 4.11 Snapshots of mixing conditions around $x = 8$ mm (downstream) in a microchannel. (a) No vibration; (b) strong vibration with $f_b = 92$ Hz [34].

tubes connected to the channel before flowing into a microchannel. The results show that fluid mixing and chemical reaction are extremely promoted by the applied vibration technique. They emphasized that the mixing rate is well correlated with the maximum r.m.s. value of normalized fluid velocity fluctuation in a microchannel [34].

Figure 4.11 shows two snapshots of the mixing conditions at $x = 8$ mm downstream of a Y-shaped microchannel in a non-vibrating case (a) , i.e. $f_b = 0$ Hz and a vibrating $f_b = 92$ Hz flow (b). It is obvious that the two fluids in a non-vibrating flow are almost completely separated, although fluid mixing is slightly progressed at the center of the channel through molecular diffusion. On the other hand, fluid mixing is noteworthy in the vibrating flow and almost complete mixing is accomplished.

Matsumoto *et al.* [35] have inferred and verified an optical measuring technique for the species concentration field in a liquid microchannel flow. The recorded fluorescence intensity is averaged along the optical path and provides a height-averaged concentration field. The measured concentration fields, and particularly concentration profiles across the microchannel, confirm both good spatial resolution and good accuracy, even for the concentration gradients within the concentration boundary layer.

Due to the application of a confocal laser scanning microscope, not only a height-averaged concentration field is attainable, as shown in [35], but also the concentration distribution of a species along the channel depth for quantitative analysis [33].

In order to obtain 3D information on the concentration field with high spatial resolution, the use of confocal microscopy (CLSM) is indispensable. The major advantage of a CLSM is the possibility of collecting emitted light only from the focus plane. A pinhole is arranged in front of the detector (photomultiplier), on a plane conjugate to the focal plane of the objective. Light coming from planes above or below the focal plane is out of focus when it strikes the pinhole. Therefore most of the light cannot pass the pinhole and does not lead to the formation of the image [36]. This spatial filtering is the key principle for increasing the optical resolution by producing

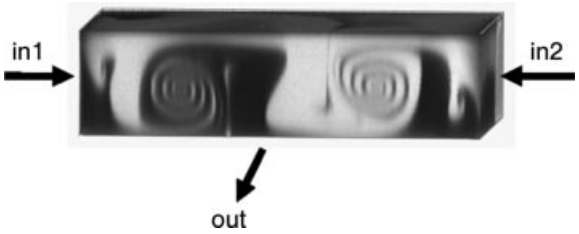

Figure 4.12 Three-dimensional concentration field, T-shaped micromixer, cross-section geometry $400 \times 100\,\mu m^2$ – beginning of the mixing channel ($Re = 130$).

depth-wise optical slicing. The illuminating laser can rapidly scan from point to point on a single focal plane, in a synchronized way with the aperture, in order to complete a full-field image on the detector unit.

Pioneering work on the use of a confocal laser scanning microscope to visualize concentration distributions along the vertical cross-sections of a mixing channel was published by Stroock *et al.* [37]. They investigated the 3D twisting flow in a channel where this mixing channel consists of patterns of grooves on the floor of the channel, referred to as a staggered herringbone mixer (SHM).

Other groups, such as Yamaguchi *et al.*, used the 3D observation of a confocal fluorescence microscope to validate simulation results. They investigated the fluidic behavior of laminar liquid flows in microchannels with hairpin curves [38]. Furthermore, Chang *et al.* used for their investigation of the flow structures a 3D hydrodynamic focusing microfluidic device. In this device, a sample flow stream was first vertically constrained into a narrow stream, and then horizontally focused on one small core region from a cross-section perspective, which is useful for cell/particle counting. They reported numerical and experimental results of the focused stream shape from a cross-section perspective, whereas the experimental images were captured using a confocal fluorescence microscope [39].

The use of CLSM also allows the visualization of the species distribution in all three dimensions. Figure 4.12 depicts the 3D concentration field at the beginning of the mixing channel in a T-shaped micromixer.

4.4.2 Analysis of Temperature Fields

A novel measurement technique using a fluorescent dye in combination with μ-PIV has been devised to investigate convective mixing in microspace. Tris(bipyridine) ruthenium(II), whose fluorescent intensity, when excited by ultraviolet light, is strongly temperature dependent, was applied to the bottom surface of a glass cover that served as the upper boundary surface of a flow channel. This setup thus realized a 2D temperature measurement of the microflow channel. A spatial resolution of $5 \times 5\,\mu m^2$ and a temperature resolution of 0.26 K were achieved by using a cooled CCD camera and a $10 \times$ objective lens of a microscope. Pure water at

different temperatures was injected into opposite inlets of a T-shaped microchannel bound by a cover glass and PDMS. The mixing process in the junction area was visualized by the present temperature and μ-PIV techniques. The convective heat flux was calculated from measurement of velocity and temperature and compared with the heat conduction. It was found that the heat flux due to conduction was larger than that due to convection, hence it was suggested that heat conduction may be an important factor in the design process of microfluidic devices [40].

It is also possible to use μ-PIV for temperature measurements. The technique is based on the precondition that Brownian motion will cause width-wise broadening of the cross-correlation peak. A correlation-based PIV algorithm detects the magnitude of Brownian particle motion and can be used to determine the temperature of the fluid [41].

Further details concerning the microparticle image thermometry can be found in [3].

4.4.3 Visualization of Mixing Processes Without Chemical Reactions

For quantitative analysis, Danckwerts' intensity of segregation I_s is used. The mixing quality M:

$$M = 1 - \sqrt{I_S} = 1 - \frac{\sigma}{\sigma_{max}} \tag{4.17}$$

can be calculated by means of the gray values of the cross-sectional areas along the mixing channel length (σ: standard deviation; σ_{max}: maximum standard deviation). A value of 0 for M corresponds to a totally segregated system whereas a value of 1 corresponds to a homogeneous mixture.

As mentioned, for example in [42], the mixing quality is not sensitive to the length scales on which the segregation takes place. Additional to the use of the mixing quality, the application of the potential for diffusive mixing Φ:

$$\Phi(V) = \frac{1}{|V|} \int_V ||\nabla f|| \, \mathrm{d}V \text{ with } f = \frac{c}{c_{max}} \tag{4.18}$$

where c is the concentration of the species is necessary. This potential for diffusive mixing is a significant parameter for the total driving force for diffusive dissipation of concentration gradients within the concentration field.

Results concerning the development of the mixing quality and the potential for diffusive mixing against the *Re* and the mixing channel length for several T-shaped micromixers can be found in [33].

4.4.4 Visualization of Reactive Mixing

It is possible to visualize not only the concentration distribution of a scalar (e.g. Rhodamine B) in a non-reacting case but also the product distribution of a

chemical reaction. Until now, neutralization reactions (instantaneous reaction) or the reaction between calcium and a fluorescent dye (with a time constant of approximately $10^9\,\mathrm{l\,mol^{-1}\,s^{-1}}$) are used. In the case of a neutralization reaction, the practical implementation consists of the utilization of the dye disodium fluorescein. The fluorescence, i.e. the quantum yield of the fluorescent dye, is dependent on the pH value and thus depends on the local chemical surroundings.

Recently, the monitoring of chemical reactions within microreactors using an inverted Raman microscope spectrometer have been reported. An inverted Raman microscope spectrometer has been used to profile the spatial evolution of reactant and product concentrations for a chemical reaction within a microreactor. The Raman spectrometer was equipped with a laser source with a wavelength of 780 nm, confocal optics, a holographic transmission grating and a charge-coupled device (CCD) detector. In this investigation, the synthesis of ethyl acetate from ethanol and acetic acid was analyzed as a model system within the microreactor. Raman scattering bands for each reactant and product species were clearly resolved. The main advantage is that the Raman spectral intensities of each band are proportional to the concentration of each species and hence all concentrations can be quantitatively measured after calibration. It is noteworthy that Raman microscopy provides a useful complementary technique to UV/VIS absorbance and fluorescence methods for the *in situ* monitoring and analysis of chemical reaction species [43].

Ichiyanagi *et al.* [44] used a simultaneous measurement technique for the analysis of the velocity and pH distribution by means of a confocal microscope and a 3CCD color camera for investigations of a chemical reacting flow field in a microchannel. Micro-PIV and micro-LIF (dye fluorescein sodium salt) were utilized for velocity and pH measurement, respectively. The advantages of the present system are the separation of the fluorescence of the particles from that of the dye by using the 3CCD color camera and the confocal microscope to provide a depth resolution of 5.0 μm. The measurement uncertainties of the pH measurements were estimated to be pH 0.23. Two aqueous solutions at different pH values were introduced into a T-shaped microchannel. The mixing process in the junction area was investigated by the present technique and the effect of the chemical reaction on the pH gradient was discussed by a comparison between the proton concentration profiles obtained from the experimental pH distribution and those calculated from the measured velocity data [44].

Furthermore, the interaction between chemical reactions and the flow field in a Y-shaped micromixer were investigated by Shinohara and co-workers. In addition, the micro-LIF technique was applied to the measurement of pH distributions in a chemically reacting flow, [45, 46].

In order to visualize the reaction-diffusion process of a second-order reaction in a T-shaped micromixer, Baroud *et al.* used the reaction between Ca^{2+} and CaGreen, a fluorescent tracer for calcium. The experimental measurements were compared with the 2D numerical simulation of the reaction–diffusion equations and showed good agreement between theory and experiment. From this study, it is possible to extract

various quantities, such as the important kinetic rate of the reaction in conditions yet inaccessible to conventional (macroscale) methods [47].

In order to visualize the chemical product in a reacting flow, a Rhod-2 solution and a calcium chloride (CaCl2) solution were used as the reactive species A and B, respectively. Rhod-2 is a fluorochrome that has a Rhodamine moiety, and it fluoresces by chelating with a Ca^{2++} ion. Hence, the complex ion produced can be visualized as a chemical product by LIF. The reaction rate constant between both reactants Rhod-2 and $CaCl_2$ is in the order of $10^6\,m^3\,mol^{-1}\,s^{-1}$, hence the reaction can be regarded as a rapid reaction.

The vibration technique for promoting fluid mixing described earlier (Section 4.4.1) shows that the chemical product is produced only in the central region of the microchannel in the non-vibrating flow. On the other hand, the chemical product is produced in the entire region of the channel in the vibrating flow. These results show that fluid mixing and chemical reaction are remarkably promoted by the proposed vibration technique [34].

Another result is given in Figure 4.13, where the product distribution of the reaction Ca^{2++} Fluo-4 is presented. The chemical product is visualized in a T-shaped micromixer with a cross-section $600 \times 300\,\mu m^2$.

The product distribution along the vortex pair in both images also depicts the 3D flow structure for higher *Re* in T-shaped micromixers.

Only very few publications have appeared concerning the concentration fields within particles in microchannels. For visualization of the concentration distribution within a slug, Burns and Ramshaw used a neutralization reaction of KOH with a acetic acid with a pH indicator that changed from pink to yellow in the aqueous phase [18].

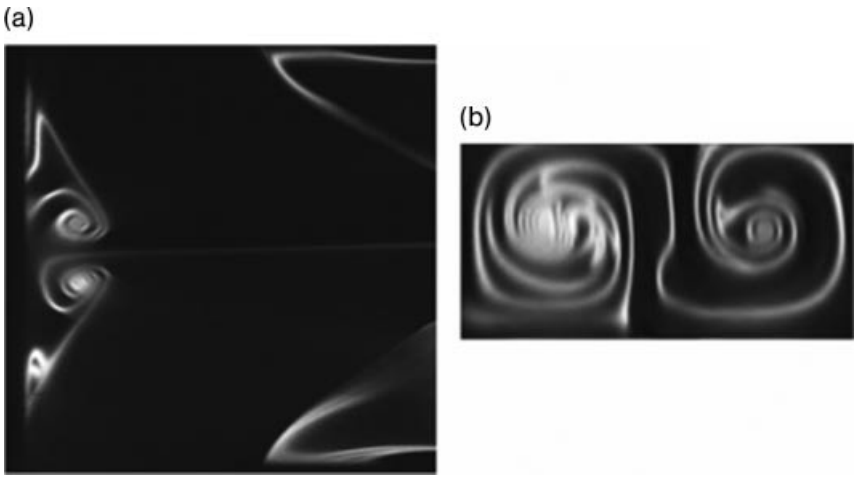

Figure 4.13 Reaction Ca^{2++} Fluo-4 (fluorescence tracer): visualization of the chemical product; T-shaped micromixer–cross-section $600 \times 300\,\mu m^2$, $Re = 186$; product distribution–horizontal slice (a), product distribution along the cross-sectional area – 4 mm downstream (b).

4.5 Conclusion

Microscale flow visualization has become an important tool for characterizing the performance of microchannels, micromixers and microreactors. Due to the rapid improvement in computer power and the great efforts in optical instrumentation, new measuring systems with high spatial and temporal resolution are available even for smaller companies and research institutes. In connection with the recent success in numerical simulation of microscale flow, a significant acceleration in clarification of microscale phenomena and technical development can be expected. By ensuring the development of reliable systems, microscale flow visualization will provide an important contribution to the further spread of micro process engineering applications in the chemical and biochemical industries.

References

1 S. Inoué, K. R. Spring, *Video Microscopy: the Fundamentals*, 2nd edn. Plenum Press, New York, **1997**.

2 M. Raffel, C. E. Willert, S. T. Wereley, J. Kompenhans, *Particle Image Velocimetry: a Practical Guide*, 2nd edn. Springer, Berlin, **2007**.

3 S. T. Wereley, C. D. Meinhart, Micron-resolution particle image velocimetry. In *Microscale Diagnostic Techniques*, ed. K. S. Breuer, Springer, Berlin, **2005**, Chapter 2.

4 M. Hoffmann, M. Schlüter, N. Räbiger, Untersuchung der Mischvorgänge in Mikroreaktoren durch Anwendung von Micro-LIF und Micro-PIV. *Chem. Ing. Tech.*, **2007**, *79* (7), 1067–1075.

5 J. M. M. Sousa, Turbulent flow around a surface mounted obstacle using 2D-3C DPIV. *Exp. Fluids*, **2002**, *33* (6), 854–862.

6 M. R. Bown, J. M. MacInnes, R. W. K. Allen, Three-component micro-PIV using the continuity equation and a comparison of the performance with that of stereoscopic measurements. *Exp. Fluids*, **2007**, *42* (2), 197–205.

7 A. K. Prasad, R. J. Adrian, C. C. Landreth, P. W. Offutt, Effect of resolution on the speed and accuracy of particle image velocimetry interrogation. *Exp. Fluids*, **1992**, *13* (2), 105–116.

8 R. J. Adrian, C. S. Yao, Pulsed laser technique application to liquid and gaseous flows and the scattering power of seed materials. *Appl. Opt.*, **1985**, *24* (1), 44–52.

9 R. J. Adrian, Particle-imaging techniques for experimental fluid mechanics. *Ann. Rev. Fluid Mech.*, **1991**, *23* (1), 261–304.

10 C. D. Meinhart, S. T. Wereley, The theory of diffraction-limited resolution in microparticle image velocimetry. *Meas. Sci. Technol.*, **2003**, *14* (7), 1047–1053.

11 M. G. Olsen, R. J. Adrian, Out-of-focus effects on particle image visibility and correlation in particle image velocimetry. *Exp. Fluids*, **2000**, *29* (7), S166–S174.

12 R. Lindken, J. Westerweel, B. Wieneke, Stereoscopic micro particle image velocimetry. *Exp. Fluids*, **2006**, *41* (2), 161–171.

13 M. M. Mielnik, L. R. Saetran, Selective seeding for micro-PIV. *Exp. Fluids*, **2006**, *41* (2), 155–159.

14 R. Luo, X. Y. Yang, X. F. Peng, Y. F. Sun, Three-dimensional tracking of fluorescent particles applied to micro-fluidic measurements. *J. Micromech. Microeng.*, **2006**, *16* (8), 1689–1699.

15 K. Shinohara, Y. Sugii, A. Aota, A. Hibara, M. Tokeshi, T. Kitamori, K. Okamoto,

High-speed micro-PIV measurements of transient flow in microfluidic devices. *Meas. Sci. Technol.*, **2004**, *15* (10), 1965–1970.

16 J. Kobayashi, Y. Mori, K. Okamoto, R. Akiyama, M. Ueno, T. Kitamori, S. Kobayashi, A microfluidic device for conducting gas–liquid-solid hydrogenation reactions. *Science*, **2004**, *304* (5675), 1305–1308.

17 E. Klemm, H. Döring, A. Geisselmann, and S. Schirrmeister, Mikrostrukturreaktoren für die heterogene Katalyse. *Chem. Ing. Tech.*, **2007**, *79* (6), 697–706.

18 J. R. Burns, C. Ramshaw, The intensification of rapid reactions in multiphase systems using slug flow in capillaries. *Lab Chip*, **2001**, *1* (1), 10–15.

19 Y. Önal, M. Lucas, P. Claus, Einsatz eines Kapillar-Mikroreaktors für die selektive Hydrierung von ungesättigten Aldehyden in der wässrigen Mehrphasenkatalyse. *Chem. Ing. Tech.*, **2005**, *77* (1–2), 101–106.

20 W. Salman, A. Gavriilidis, P. Angeli, Axial mass transfer in Taylor flow through circular microchannels. *AIChE J.*, **2007**, *53* (6), 1413–1428.

21 E. R. Murphy, J. R. Martinelli, N. Zaborenko, S. L. Buchwald, K. F. Jensen, Accelerating reactions with microreactors at elevated temperatures and pressures: profiling aminocarbonylation reactions. *Angew. Chem.*, **2007**, *119* (10), 1764–1767.

22 D. Malsch, M. Kielpinski, R. Merthan, J. Albert, G. Mayer, J. M. Köhler, H. Süsse, M. Stahl, T. Henkel, PIV-analysis of Taylor flow in micro channels. *Chem. Eng. J.*, **2008**, *135* (Supplement 1), S166–S172.

23 R. J. Adrian, K. T. Christensen, Z. -C. Liu, Analysis and interpretation of instantaneous turbulent velocity fields. *Exp. Fluids*, **2000**, *29* (3), 275–290.

24 R. Lima, S. Wada, K. Tsubota, T. Yamaguchi, Confocal micro-PIV measurements of three-dimensional profiles of cell suspension flow in a square microchannel. *Meas. Sci. Technol.*, **2006**, *17* (4), 797–808.

25 H. Kinoshita, S. Kaneda, T. Fujii, M. Oshima, Three-dimensional measurement and visualization of internal flow of a moving droplet using confocal micro-PIV. *Lab Chip*, **2007**, *7* (3), 338–346.

26 M. R. Bown, J. M. MacInnes, R. W. K. Allen, W. B. J. Zimmerman, Three-component micron resolution velocity measurements using sterescopic micro-PIV. In Proceedings of the 6th International Symposium on Particle Image Velocimentry, **2005**, S06.

27 S. Kim, S. J. Lee, Measurement of 3D laminar flow inside a micro tube using micro digital holographic particle tracking velocimetry. *J. Micromech. Microeng.*, **2007**, *17* (10), 2157–2162.

28 C.-T. Yang, H.-S. Chuang, Measurement of a microchamber flow by using a hybrid multiplexing holographic velocimetry. *Exp. Fluids*, **2005**, *39* (2), 385–396.

29 M. Speidel, A. Jonáš, E. L. Florin, Three-dimensional tracking of fluorescent nanoparticles with subnanometer precision by use of off-focus imaging. *Opt. Lett.*, **2003**, *28* (2), 69–71.

30 M. Wu, J. W. Roberts, M. Buckley, Three-dimensional fluorescent particle tracking at micron-scale using a single camera. *Exp. Fluids*, **2005**, *38* (4), 461–465.

31 J. S. Park, K. D. Kihm, Three-dimensional micro-PTV using deconvolution microscopy. *Exp. Fluids*, **2006**, *40* (3), 491–499.

32 D. Sinton, Microscale flow visualization. *Microfluids Nanofluids*, **2004**, *1*, 2–21.

33 M. Hoffmann, M. Schlüter, N. Räbiger, Experimental investigation of liquid–liquid mixing in T-shaped micro-mixers using μ-LIF and μ-PIV. *Chem. Eng. Sci.*, **2006**, *61* (9), 2968–2976.

34 Y. Ito, S. Komori, A vibration technique for promoting liquid mixing and reaction in a microchannel. *AIChE J.*, **2006**, *52* (9), 3011–3017.

35 R. Matsumoto, H. F. Zadeh, P. Ehrhard, Quantitative measurement of depth-averaged concentration fields in

microchannels by means of a fluorescence intensity method. *Exp. Fluids*, **2005**, *39* (4), 722–729.

36 S. Wilhelm, B. Gröbler, M. Gluch, H. Heinz. Confocal laser scanning microscopy: principles. www.zeiss.de/lsm, **2003**.

37 A. D. Stroock, S. K. W. Dertinger, A. Ajdari, I. Mezić, H. A. Stone, G. M. Whitesides, Chaotic mixer for microchannels. *Science*, **2002**, *295* (5555), 647–651.

38 Y. Yamaguchi, F. Takagi, K. Yamashita, H. Nakamura, H. Maeda, K. Sotowa, K. Kusakabe, Y. Yamasaki, S. Morooka, 3-D simulation and visualization of laminar flow in a microchannel with hair-pin curves. *AIChE J.*, **2004**, *50* (7), 1530–1535.

39 C.-C. Chang, Z.-X. Huang, R.-J. Yang, Three-dimensional hydrodynamic focusing in two-layer polydimethylsiloxane (PDMS) microchannels. *J. Micromech. Microeng.*, **2007**, *17* (8), 1479–1486.

40 Y. Sato, G. Irisawa, M. Ishizuka, K. Hishida, M. Maeda, Visualization of convective mixing in microchannel by fluorescence imaging. *Meas. Sci. Technol.*, **2003**, *14* (1), 114–121.

41 V. Hohreiter, S. T. Wereley, M. G. Olsen, J. N. Chung, Cross-correlation analysis for temperature measurement. *Meas. Sci. Technol.*, **2002**, *13* (7), 1072–1078.

42 D. Bothe, C. Stemich, H.-J. Warnecke, Fluid mixing in a T-shaped micro-mixer. *Chem. Eng. Sci.*, **2006**, *61* (9), 2950–2958.

43 P. D. I. Fletcher, S. J. Haswell, X. Zhang, Monitoring of chemical reactions within microreactors using an inverted Raman microscopic spectrometer. *Electrophoresis*, **2003**, *24* (18), 3239–3245.

44 M. Ichiyanagi, Y. Sato, K. Hishida, Optically sliced measurement of velocity and ph distribution in microchannel. *Exp. Fluids*, **2007**, *43* (2–3), 425–435.

45 K. Shinohara, Y. Sugii, K. Okamoto, H. Madarame, A. Hibara, M. Tokeshi, T. Kitamori, Measurement of pH field of chemically reacting flow in microfluidic device by laser-induced fluorescence. *Meas. Sci. Technol.*, **2004**, *15* (5), 955–960.

46 K. Shinohara, Y. Sugii, A. Hibara, M. Tokeshi, T. Kitamori, K. Okamoto, Rapid proton diffusion in microfluidic devices by means of micro-LIF technique. *Exp. Fluids*, **2005**, *38* (1), 117–122.

47 C. N. Baroud, F. Okkels, L. Ménétier, P. Tabeling, Reaction–diffusion dynamics: confrontation between theory and experiment in a microfluidic reactor. *Phys. Rev. E*, **2003**, *67* (4), 060104.